Published by Avanti Publishers

Journal of Chemical Engineering Research Updates

ISSN (online): 2409-983X

Investigation of Gas-Solid Flows in a Spout Fluidized Bed on Drag and Solid Stress: CFD-DEM, TFM, and Experimental Validation

Xinyao Guo, Guodong Liu*, Junnan Zhao, Runchun Wang and Yurong He

School of Energy Science and Engineering, Harbin Institute of Technology, Harbin 150001, China

ARTICLE INFO

Article Type: Research Article

Keywords:
TFM
CFD-DEM
Drag model
Spout fluidized bed
Friction stress model

Timeline:
Received: June 28, 2021
Accepted: August 31, 2021
Published: September 22, 2021

Citation: Guo X, Liu G, Zhao J, Wang R, He Y. Investigation of Gas-solid Flows in a Spout Fluidized Bed on Drag and Solid Stress: CFD-DEM, TFM, and Experimental Validation. J Chem Eng Res Updates, 2021; 8: 1-23.

DOI: https://doi.org/10.15377/2409-983X.2021.08.1

ABSTRACT

In this work, experimental and numerical simulation methods are used to study the gas-solid two-phase flow in a three-dimensional rectangular spouted bed. In particular, the TFM and the CFD-DEM simulation results are compared with experimental data of the spouted bed. The influence of different drag models and friction stress models on the applicability of the simulation technology, Gidaspow, BVK, Koch-Hill, and Syamal-O'Brein drag models are investigated, respectively. Besides, the influence of the Syamal (S-R-O) and Srivastava-Sundaresan (S-S) friction stress models considering different transition points on the flow characteristics of particles in a spouted bed is also studied. Experimental verification shows that the Gidaspow drag, and S-S friction stress models are more consistent with experimental results. The fountain height predicted by CFD-DEM is closer to the experiment. It is found that the heterogeneous flow structure resulted in such a phenomenon in that the bubble cap blocked the gas flow pathway and increased the drag coefficient, while the bypass of the gas phase near the walls in the bubble reduced the drag coefficient.

*Corresponding Author
Email: gdliu@hit.edu.cn
Tel: +86-18845022080

1. Introduction

Fluidized bed reactors have been widely used in many industrial applications, such as gasification, cracking, combustion, synthesis reactions, other chemical reactions, and metallurgical engineering [1]. The Spout Fluidized Bed (SFB), designed initially to dry bulk cereals, is a special type of fluidized bed [2]. Compared with other fluidized beds, SFB is characterized by the fluidization of particles, low operating pressure, and high gas-solid contact efficiency of coarse particles.

At present, the main research methods of gas-solid two-phase flow are experiment and numerical simulation [3]. The numerical models used to study gas-solid SFB are mainly divided into the two-fluid model (TFM) based on the Euler-Euler method and discrete element model (CFD-DEM) based on Euler- Lagrange method. In the TFM model, the particle phase and the fluid phase are concerned as the continua which could coexist and penetrate each other. These momentum equations are usually closed by the kinetic theory of granular flows(KTGF) [4,5]. The Euler-Lagrange model allows an individual or group tracking of solid particles according to Newton's theorem of the particles' motion. For the discrete phase simulation, particle-particle and particle-wall collisions can be stochastically modeled. In the dense regime, the hard-sphere and soft-sphere models have been developed according to the different handling modes (rigidity or deformability) of particles during the collision. The collision in the hard-sphere model is assumed to be a binary instantaneous elastic collision. The soft-sphere model assumes that the collision is a non-instantaneous inelastic collision, allowing particles to overlap or penetrate the wall (depending on the penetration depth) to determine the movement of the particles that change the contact force [6,7]. However, as the number of particles increases, the computational cost of trajectory analysis will be very high, so this method is suitable for laboratory-scale simulations currently [8].In the framework of the CFD-DEM, some studies have been conducted to simulate the hydrodynamics of gas-solid two-phase flows in cold SFB. Zhao *et al*. [9] used CFD-DEM to simulate a rectangular spouted bed with a thickness of 15 mm and compared the simulation with the experimental data from the particle image velocimetry. Based on the CFD-DEM method, Saidi *et al*. [10] simulated the gas-solid two-phase flow in a rectangular SFB and studied the effects of column thickness, two-dimensional and three-dimensional CFD simulations on the flow field and particles' motions. Marchelli *et al*. [11] conducted extensive sensitivity analysis on the CFD-DEM simulation of spouted beds, they showed that the drag model, restitution coefficient, friction coefficient, and the Magnus lift model have the greatest influence on the particle motion trajectory. In addition, researchers have not reached a consensus on selecting some physical aspects (drag force models) for SFB [11]. At present, the sensitivity analysis of CFD-DEM simulation on SFB is few, and the conclusions obtained in the drag part are quite different. Li *et al*. [12] found that van der Hoef [13] and Gidaspow [14] models can better predict bubble formation, and BVK [15] model can better predict the fluidization process of spouted bed. Pietsch *et al*. [16] simulated a three-dimensional prismatic spouted bed and showed Koch and Hill [13] and Beetstra [15] drag models reproduced experimentally observed spouting behavior.

Compared with CFD-DEM, the TFM method has less resource requirement. Consequently, the TFM method can be frequently used to simulate the actual jet flow [17]. Du *et al*. [18,19] studied the effects of gas-solid drag model, friction stress, maximum packing limit on SFB using the TFM and found that the Gidaspow [14] drag model provided the best fits to the experimental data. It was also found that frictional stress was important in the annulus. A higher maximum packing limit would increase particle velocity and a slight increase in bed voidage. Moliner *et al*. [20] conducted a numerical simulation of a spouted bed based on the TFM method and verified it with experimental data. It was concluded that the exact choice of the drag model had the greatest influence, and the specularity coefficient and restitution coefficient also played an important role in optimizing the model. Furthermore, for a spouted bed, Moliner *et al*. [8] and Stroh *et al*. [21] reported that the CFD-DEM was more accurate than the TFM model in overall prediction.

The above studies have shown that both CFD-DEM and TFM can predict the complicated gas-solid two-phase flow, but they did not examine the ability of the two strategies to reproduce the flow pattern and the difference in the SFB when the flow pattern is changed. The main objective of the present work is to compare the simulation of gas-solid two-phase flow in a spouted bed using both the TFM and the CFD-DEM methods to analyze the sensitivity of the TFM models. Firstly, in the CFD-DEM simulation, we assume that the apparent velocity is 1.5 u_{mf} ,

and compare the simulated conditions of spouted bed with different drag models with the experiment data to get the most suitable drag model. Then, in the TFM simulation, by comparing the effects of different restitution coefficients on the flow behavior of the spouted bed, the effect of the friction stress model is considered. Finally, the simulation results of the CFD-DEM and the TFM for gas-solid two-phase flow in the SFB are compared at three apparent velocities. The differences between the simulation results are analyzed and discussed subsequently.

2. Mathematical and Numerical Methods

2.1. Euler-Euler Two-Fluid Model

The TFM considers particles and fluid as continuous media, and each of them follows its mass, momentum, and energy transfer equations. Both phases are coupled to each other by interphase forces and a common pressure field. In TFM, the simulation of solid stress is based on the (KTGF) [14]. The particle velocity can be decomposed into a local averaged velocity $\langle \vec{u}_s \rangle$ and a superposition wave component (pulsation velocity) $\vec{c}_s$ to represent the particle's pulsation. So, $\vec{u}_s = \langle \vec{u}_s \rangle + \vec{c}_s$. The viscous force and solid pressure of the particles can be expressed as a function of the granular temperature. The governing equations for the TFM are summarized in Table **A1**.

2.2. CFD-DEM

In the CFD-DEM, the continuous phase still obeys the mass and momentum conservation equations [25]. The behavior of the gas phase is described similarly to for the TFM given in Table **A1**. However, the treatment of the solid phase is quite different. The essence of CFD-DEM is to treat each particle as a discrete element and predict its behavior by its Newton equation of motion. Particles are subjected to a combination of forces, including gravity, drag, and contact forces. The contact forces consist of particle-particle and particle-wall collisions, which are treated by the soft sphere method using the linear spring-damper model proposed by Cundall and Strack [6], as shown in Figure **1**. The spring causes the rebound of the colliding particles, and the damper represents the kinetic energy dissipation caused by the inelastic collision. The governing equations and contact force models of the CFD-DEM are indicated in Table **A2**.

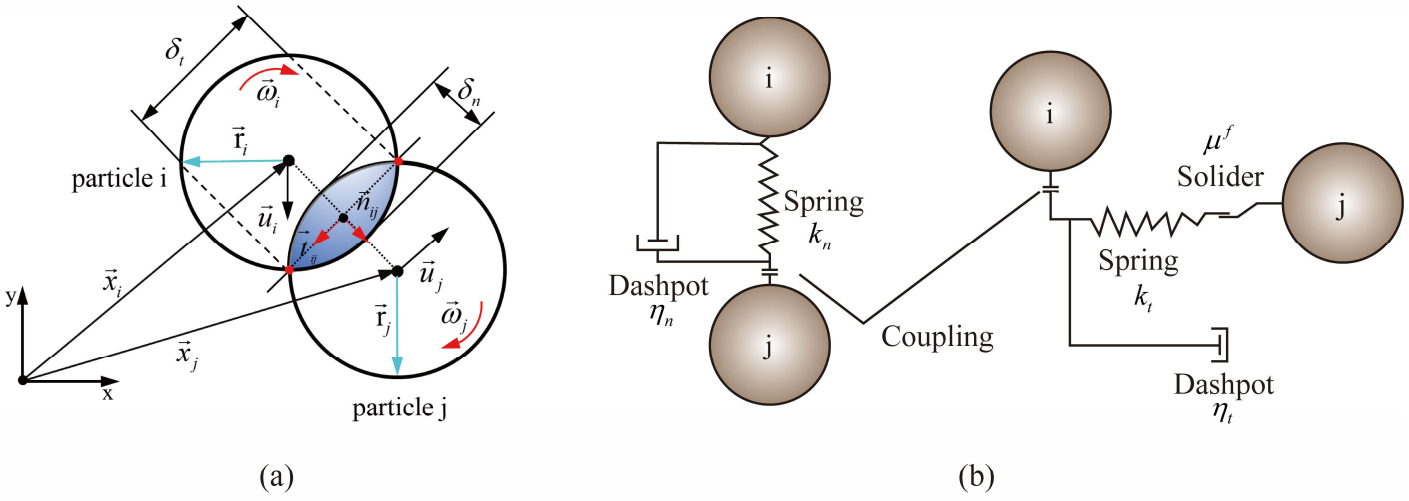

Figure 1: (a) particle-particle collision (b) the spring-damper-slider system.

Many researchers have studied the momentum exchange between the gas and solid phases in the CFD-DEM [9,26-29]. The empirical formula of the momentum exchange coefficient is similar to that in the TFM.

Table A1: The governing equations and constitutive closures of the TFM.

Continuity equations:

Gas-phase: $\frac{\partial}{\partial t}\left(\varepsilon_g\rho_g\right)+\nabla\cdot\left(\varepsilon_g\rho_g\vec{u}_g\right)=0$

Solid-phase: $\frac{\partial}{\partial t}\left(\varepsilon_s\rho_s\right)+\nabla\cdot\left(\varepsilon_s\rho_s\vec{u}_s\right)=0$

Momentum equations:

Gas-phase: $\frac{\partial}{\partial t}\left(\varepsilon_g\rho_g\vec{u}_g\right)+\nabla\cdot\left(\varepsilon_g\rho_g\vec{u}_g\vec{u}_g\right)=\nabla\cdot\overline{\overline{\tau}}_g+\varepsilon_g\rho_g\vec{g}-\varepsilon_g\nabla p_g-\beta_{gs}(\vec{u}_g-\vec{u}_s)$

Solid-phase: $\frac{\partial}{\partial t}\left(\varepsilon_s\rho_s\vec{u}_s\right)+\nabla\cdot\left(\varepsilon_s\rho_s\vec{u}_s\vec{u}_s\right)=\nabla\cdot\overline{\overline{\tau}}_s+\varepsilon_s\rho_s\vec{g}-\varepsilon_s\nabla p_g-\nabla p_s+\beta_{gs}(\vec{u}_g-\vec{u}_s)$

Gas-phase stress tensor: $\overline{\overline{\tau}}_g=\varepsilon_g\mu_g\left[\nabla\vec{u}_g+(\nabla\vec{u}_g)^{\mathrm{T}}\right]-\frac{2}{3}\varepsilon_g\mu_g(\nabla\cdot\vec{u}_g)\overline{\overline{I}}$

Granular temperature: $\theta=\frac{1}{3}\left\langle\vec{c}_s\cdot\vec{c}_s\right\rangle$

Granular temperature equation: $\frac{3}{2}\left[\frac{\partial}{\partial t}\left(\varepsilon_s\rho_s\theta\right)+\nabla\cdot\left(\varepsilon_s\rho_S\theta\vec{u}_s\right)\right]=\left(-p_{kc}\overline{\overline{I}}+\overline{\overline{\tau}}_{kc}\right):\nabla\vec{u}_s+\nabla\cdot\left(\kappa_s\nabla\theta\right)-\gamma_s$

Diffusion coefficient of granular energy: (Gidaspow *et al*. [14])

$$\kappa_s=\frac{150\rho_s d_s(\theta\pi)^{1/2}}{384g_0(1+e)}\left[1+\frac{6}{5}g_0\varepsilon_s(1+e)\right]^2+2\varepsilon_s^2\rho_s d_s g_0(1+e)\left(\frac{\theta}{\pi}\right)^{1/2}$$

Collision energy dissipation: (Lun *et al*. [22])

$$\gamma_s=\frac{12(1-e^2)g_0}{d_s\pi^{1/2}}\rho_s\varepsilon_s^2\theta^{3/2}$$

Radial distribution function: (Carnahan and Starling. [23])

$$g_0=\frac{1-0.5\varepsilon_s}{(1-\varepsilon_s)^3}$$

Solid-phase pressure and Stress tensor: (Johnson and Jackson. [24]）

$p_s=p_{kc}+p_f$ $\overline{\overline{\tau}}_s=\overline{\overline{\tau}}_{kc}+\overline{\overline{\tau}}_f$

Kinetic-collision stress tensor: $\overline{\overline{\tau}}_{kc}=\mu_b(\nabla\cdot\vec{u}_s)\overline{\overline{I}}+\mu_{kc}\left[\nabla\vec{u}_s+(\nabla\vec{u}_s)^{\mathrm{T}}\right]-\frac{2}{3}(\nabla\cdot\vec{u}_s)\overline{\overline{I}}$

Frictional stress tensor: $\overline{\overline{\tau}}_f=\mu_f\left[\nabla\vec{u}_s+(\nabla\vec{u}_s)^{\mathrm{T}}\right]-\frac{2}{3}(\nabla\cdot\vec{u}_s)\overline{\overline{I}}$

Kinetic-collision for solid-phase: (Lun *et al*. (1984) [22])

$$p_{kc}=\left[1+2\varepsilon_s(1+e)g_0\right]\rho_s\varepsilon_s\theta$$

Bulk viscosity: (Lun *et al*. (1984) [22])

$$\mu_b=\frac{4}{3\pi^{1/2}}\varepsilon_s^2(1+e)g_0\rho_s d_s\theta^{1/2}$$

Shear viscosity: (Lun *et al*. (1984) [22])

$$\mu_{kc}=\left(\frac{2+\alpha}{3}\right)\left[\frac{5\pi^{1/2}}{24(1+e)(3-e)g_0}\left(1+\frac{4}{5}(1+e)\varepsilon_s g_0\right)\left(1+\frac{2}{5}(1+e)(3e-1)\varepsilon_s g_0\right)+\frac{8}{5\pi^{1/2}}(1+e)\varepsilon_s^2 g_0\right]\rho_s d_s\theta^{1/2}$$

Where $\alpha=1.6$

Table A2: Governing equations and contact force models of the CFD-DEM.

Translation equation:

$$m_i \frac{d\vec{u}_i}{dt} = m_i \vec{g} + \vec{F}_{dra,i} + \left(\vec{f}_{ij}^{\,n} + \vec{f}_{ij}^{\,t} \right)$$

Rotation equation:

$$I_i \frac{d\vec{\omega}_i}{dt} = \vec{T}_i = \sum_{\substack{j=1 \\ j \neq i}}^{N} \left(\mathrm{r}_i \vec{\eta}_{ij} \times \vec{f}_{ij}^{\,t} \right)$$

Normal overlapping area:

$$\delta_n = \mathrm{r}_i + \mathrm{r}_j - \left| \vec{x}_j - \vec{x}_i \right|$$

Normal vector:

$$\vec{n}_{ij} = \frac{\vec{x}_j - \vec{x}_i}{\left| \vec{x}_j - \vec{x}_i \right|}$$

The relative velocity between colliding particles:

$$\vec{u}_{ij} = \vec{u}_i - \vec{u}_j + \left(\mathrm{r}_i \vec{\omega}_i + \mathrm{r}_j \vec{\omega}_j \right) \times \vec{n}_{ij}$$

Normal: $\vec{u}_{ij}^{\,n} = \left(\vec{u}_i - \vec{u}_j \right) \cdot \vec{n}_{ij} \vec{n}_{ij}$ Tangential: $\vec{u}_{ij}^{\,t} = \vec{u}_{ij} - \vec{u}_{ij} \cdot \vec{n}_{ij} \vec{n}_{ij}$

The normal component of the contact force:

$$\vec{f}_{ij}^{\,n} = -k_n \delta_n \vec{n}_{ij} - \eta_n u_{ij}^n$$

The tangential component of the contact force:

$$\vec{f}_{ij}^{\,t} = \begin{cases} -k_t \delta_t \vec{t}_{ij} - \eta_t u_{ij}^t \ , & \left| f_{ij}^t \right| \leq \mu^f \left| f_{ij}^n \right| \\ -\mu_f \left| f_{ij}^n \right| \ , & \left| f_{ij}^t \right| > \mu^f \left| f_{ij}^n \right| \end{cases}$$

The drag force of particle i in a grid is expressed as follows:

$$\vec{F}_{dra,i} = -\nabla p_g + \frac{\beta_{gs} \vec{u}_s}{\varepsilon_s} \left(\vec{u}_g - \vec{u}_s \right)$$

2.3. Drag Model

The correlation of momentum exchange coefficient β_{gs} is usually obtained by pressure drop measurements in a fixed bed, a fluidized bed, or a settling bed. Several drag models have been reported in the literature to calculate momentum exchange coefficients in gas-solid systems [13-15,30-32]. Note that to investigate the effects of different frictional stress models in TFM on the flow characteristics of particles in SFB, Gidaspow [14] drag models are used in this paper. In this paper, the gas-solid momentum exchange coefficients are calculated by using four different drag models, as shown in Table **B1**.

Table B1: Drag models.

Gidaspow [14]: This model is a combination of the Wen-Yu [31] model and Ergun [30] equation.

$$\beta_{\text{Gidaspow}} = \begin{cases} \beta_{\text{wen-yu}} = \frac{3}{4} C_D \frac{\rho_g \varepsilon_g \varepsilon_s \left|\vec{u}_g - \vec{u}_s\right|}{d_s} \varepsilon_g^{-2.65} & \varepsilon_g \geq 0.8 \\ \beta_{\text{Ergun}} = \frac{150\varepsilon_s \left(1-\varepsilon_g\right)\mu_g}{\varepsilon_g d_s^2} + \frac{1.75\rho_g \varepsilon_s \left|\vec{u}_g - \vec{u}_s\right|}{d_s} & \varepsilon_g < 0.8 \end{cases}$$

$$C_D = \begin{cases} \frac{24}{\text{Re}_s}\left(1 + 0.15\text{Re}_s^{0.687}\right) & \text{Re}_s \leq 1000 \\ 0.44 & \text{Re}_s > 1000 \end{cases}, \quad \text{Re}_s = \frac{\rho_g \varepsilon_g \left|\vec{u}_g - \vec{u}_s\right| d_s}{\mu_g}$$

Syamlal-O'Brein [32]: $\beta_{\text{Syamlal-O'Brein}} = \frac{3}{4}\frac{\rho_g \varepsilon_g \varepsilon_s}{V_r^2 d_s}(0.63 + 4.8\sqrt{\frac{V_r}{\text{Re}_s}})^2 \left(\frac{\text{Re}_s}{V_r}\right)\left|\vec{u}_g - \vec{u}_s\right|$

$$V_r = 0.5A - 0.03\text{Re}_s + 0.5 \times \sqrt{\left(0.06\text{Re}_s\right)^2 + 0.12\text{Re}_s(2B - A) + A^2}$$

$$A = \varepsilon_g^{4.14}, \quad B = \begin{cases} 0.28\varepsilon_g^{1.28} & \varepsilon_g \leq 0.85 \\ \varepsilon_g^{2.65} & \varepsilon_g > 0.85 \end{cases}$$

Koch-Hill [13]: $\beta_{\text{Koch-Hill}} = \frac{18\mu_g \varepsilon_g \varepsilon_s F}{d_s^2}$

$$F = \begin{cases} 1 + \frac{3}{8}\left(\frac{\text{Re}}{2}\right), & \varepsilon_s \leq 0.01 \text{ and } \frac{\text{Re}}{2} \leq \frac{F_2 - 1}{3/8 - F_3} \\ F_0 + F_1\left(\frac{\text{Re}}{2}\right)^2, & \varepsilon_s > 0.01 \text{ and } \frac{\text{Re}}{2} \leq \frac{F_3 + \sqrt{F_3^2 - 4F_1\left(F_0 - F_2\right)}}{2F_1} \\ F_2 + F_3\left(\frac{\text{Re}}{2}\right), & \text{otherwise} \end{cases}$$

$$F_0 = \begin{cases} (1-\omega)\left[\frac{1 + 3\sqrt{\varepsilon_s/2} + (135/64)\varepsilon_s \ln\varepsilon_s + 17.14\varepsilon_s}{1 + 0.681\varepsilon_s - 8.48\varepsilon_s^2 + 8.16\varepsilon_s^3}\right] + \omega\left[\frac{10\varepsilon_s}{\varepsilon_g}\right], & \varepsilon_s < 0.4 \\ \frac{10\varepsilon_s}{\varepsilon_g^3}, & \varepsilon_s \geq 0.4 \end{cases}$$

$$F_1 = \begin{cases} \frac{\sqrt{2}}{40\sqrt{\varepsilon_s}} & 0.01 < \varepsilon_s \leq 0.1 \\ 0.11 + 0.00051 \cdot e^{11.6\varepsilon_s} & \varepsilon_s > 0.1 \end{cases}$$

$$F_2 = \begin{cases} (1-\omega)\left[\frac{1 + 3\sqrt{\varepsilon_s/2} + (135/64)\varepsilon_s \ln\varepsilon_s + 17.89\varepsilon_s}{1 + 0.681\varepsilon_s - 11.03\varepsilon_s^2 + 15.41\varepsilon_s^3}\right] + \omega\left[\frac{10\varepsilon_s}{\varepsilon_g^3}\right], & \varepsilon_s < 0.4 \\ \frac{10\varepsilon_s}{\varepsilon_g}, & \varepsilon_s \geq 0.4 \end{cases}$$

$$F_3 = \begin{cases} 0.9351\varepsilon_s + 0.03667 & \varepsilon_s < 0.095 \\ 0.0673 + 0.212\varepsilon_s + 0.0232\varepsilon_g^{-5} & \varepsilon_s \geq 0.095 \end{cases} \text{ and } \omega = e^{\left[-10(0.4-\varepsilon_s)/\varepsilon_s\right]}$$

BVK [15]: $\beta_{\text{BVK}} = 18\frac{\varepsilon_s \varepsilon_g \mu_g}{d_s^2} F_0$

$$F_0 = 10\frac{\varepsilon_s}{\varepsilon_g^2} + \varepsilon_g^2\left(1 + 1.5\varepsilon_s^{0.5}\right) + \frac{0.413\text{Re}_s}{24\varepsilon_g^2}\frac{\varepsilon_g^{-1} + 3\varepsilon_s\varepsilon_g + 8.4\text{Re}_s^{-0.343}}{1 + 10^{3\varepsilon_g}\text{Re}_s^{-0.5-2\varepsilon_s}}$$

2.4. Frictional Stress Model

According to the characteristics of particle flow, the flow can be divided into three states: quasi-static flow, fast flow, and slow flow [33]. In the quasi-static flow and fast flow, solid stress can be closed by frictional stress models and KTGF [4,5]. The slow flow in the intermediate regime is due to the coexistence of both frictional stresses and dynamic stresses, so the solution of the slow flow state becomes more complicated. However, at high particle concentration, the particle dynamic stress and the particle frictional stress coexist simultaneously, so it is necessary to introduce the friction stress model to explain the persistent particle-particle contact and collision problems. In the MFIX, the dynamic part of solid stress is based on the model of Lun *et al*. [22] and frictional stress models are indicated in Table **B2**.

Table B2: Frictional stress model for the solids phase.

Syamlal(S-R-O) [34]:

Solid-phase frictional stress [34]:

$$p_f = \begin{cases} 0 & \text{if } \varepsilon_s < \varepsilon_{s,\max} \\ 10^{25}(\varepsilon_s - \varepsilon_{s,\max})^{10} & \text{if } \varepsilon_s \geq \varepsilon_{s,\max} \end{cases}$$

Solid-phase frictional viscosity: Schaeffer [35].

$$\mu_f = p_f \frac{\sqrt{2}\sin\phi}{2\sqrt{\bar{\bar{D}}_s : \bar{\bar{D}}_s}}$$

Srivastava and Sundaresan(S-S) [36]:

Solid-phase frictional stress: Johnson & Jackson (1987) [24].

$$P_f = \begin{cases} 10^{25}\left(\varepsilon_s - \varepsilon_{s,\max}\right)^{10} & \varepsilon_s > \varepsilon_{s,\max} \\ 0.05\dfrac{\left(\varepsilon_s - \varepsilon_{s,\max}\right)^2}{\left(\varepsilon_{s,\max} - \varepsilon_s\right)^5} & \varepsilon_{s,\min} < \varepsilon_s \leq \varepsilon_{s,\max} \\ 0 & \varepsilon_s \leq \varepsilon_{s,\min} \end{cases}$$

Solid-phase frictional viscosity [36]:

$$\mu_f = p_f \frac{\sqrt{2}\sin\phi}{2\sqrt{\bar{\bar{D}}_s : \bar{\bar{D}}_s + \dfrac{\theta}{d_s^2}}} \quad \bar{\bar{D}}_s = \frac{1}{2}\left[\nabla\vec{u}_s + (\nabla\vec{u}_s)^{\mathrm{T}}\right] - \frac{1}{3}(\nabla\cdot\vec{u}_s)\bar{\bar{I}}$$

3. Experiment and Numerical Simulations

3.1. Experimental Facility

The experiments with three superficial gas velocities (three different fluidization conditions) are carried out on a laboratory-scale spouted bed device. Figure **2** shows the geometrical details of the experimental apparatus, which has a height of 0.8 m, a width of 0.15 m, and a depth of 0.02 m.

The walls of the column are made of acrylic glass panels for better visualization of the particles' movement in the bed. The inlet pressure is set to be 105700 Pa, and the upper outlet is fully open to the environment to achieve a uniform air intake and suppress pressure drop fluctuations under the bed. Such conditions ensure that the air is discharged without interference. Further parameters of experiments are summarized in Table **1**. In this experiment, it is assumed that the depth of the device is small enough to achieve the pseudo-2D requirement necessary to record images using a high-resolution camera. In addition, a simple flow chart for the corresponding numerical simulation is shown in Figure **3**.

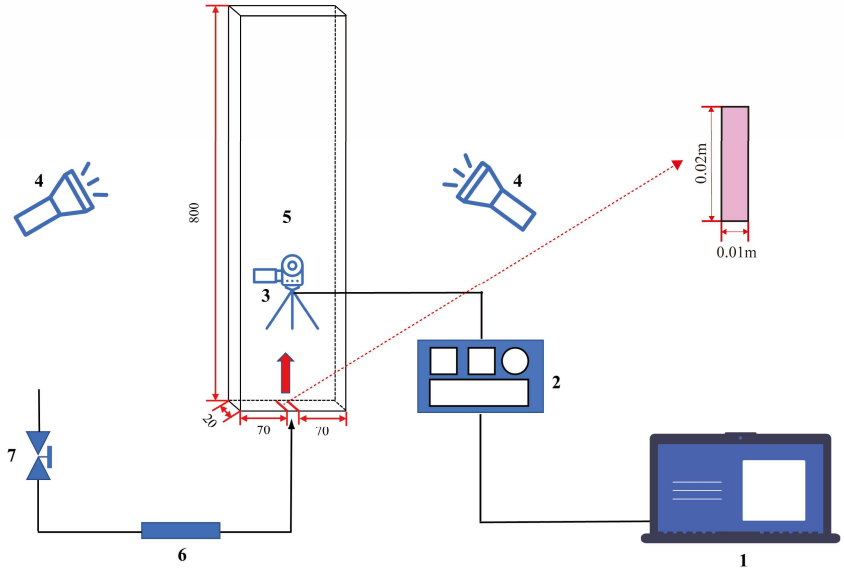

Figure 2: Schematic of the experimental set-up (unit: mm), 1—computer; 2—camera controller; 3—high-speed camera; 4—LED lights; 5—spouted bed column; 6—mass and volume controller; 7—valve.

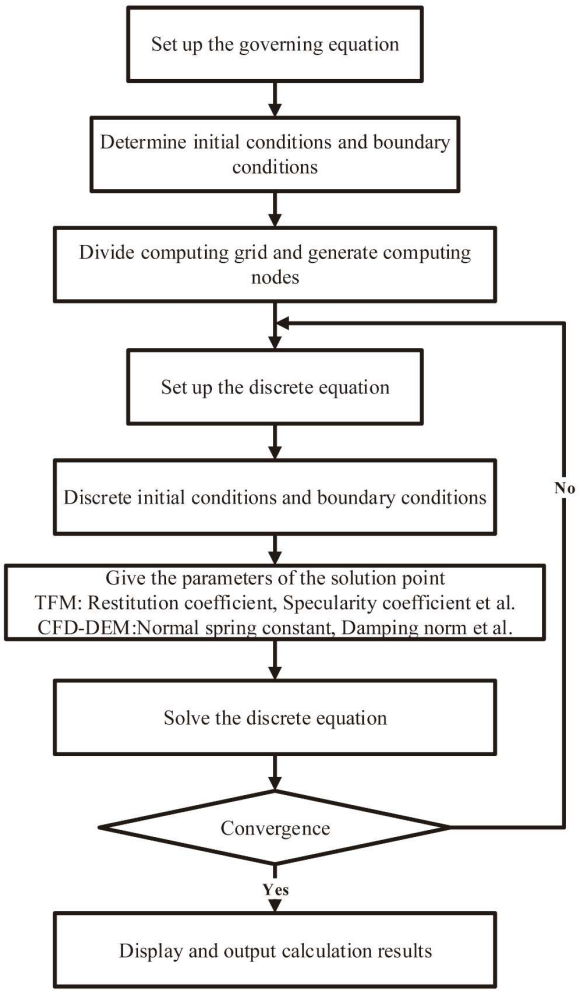

Figure 3: Simulation step-wise procedure flow chart.

Table 1: Parameters of the experimental set-up.

Gas-phase	Fluidization medium	Air
	Temperature	25℃
	Dynamic viscosity	1.827×10^{-5} kg/(m·s)
	Superficial velocity ratio (u_0/u_{mf})	1.25,1.5,1.75
Solid-phase	Geldart's particle classification	D [37]
	Total particle weight	0.65 kg
	Mean diameter	0.002 m
	Minimum fluidization velocity (u_{mf})	1.06 m/s
	Initial bed height	0.145 m

3.2. Geometry and Numerical Grid

The geometric model and the computational grid are created in the MFIX platform the same as that with the experimental configuration, and the inlet is modeled as a narrow channel. The choice of the CFD computational grid greatly influences the accuracy of the solution and the amount of work requirement. Therefore, we conduct a grid independence verification to verify the reasonable range of the number of grids. According to Figure **4**, when the number of grids exceeds 30×80×2, the calculated value does not change obviously, then the grids of 30×80×2 are selected for the following calculations. In addition, the computation of CFD-DEM is parallelized to reduce the computation time.

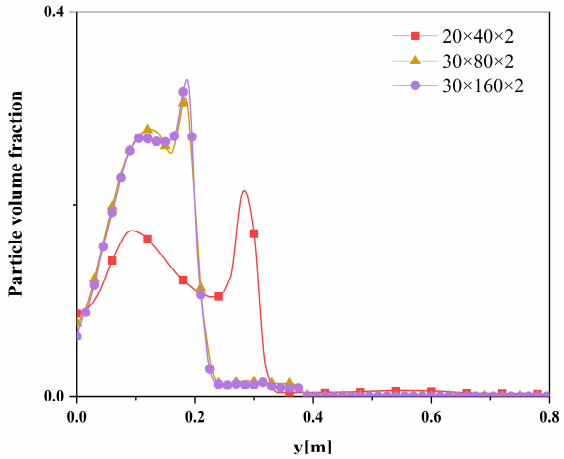

Figure 4: Grid independence test via particle volume fraction distribution along with bed height.

3.3 Boundary and Initial Conditions

Figure **5** shows the experimental conditions employed to validate the numerical simulations and the corresponding settings for both TFM and CFD-DEM. Fluidization uses room-temperature gases and a distributor located at the bottom of the bed. The velocity component of the gas phase is assumed to be uniformly distributed at the inlet. Initially, the velocity of the injected gas through the inlet increases from the minimum fluidization velocity to the required spouting velocity in an instant. Then, at three different inlet velocities, pressurized air enters into the spouted bed. The outlet is a continuous outflow of the fluid phase, and the pressure is set to be the ambient atmosphere. For the TFM, the wall boundary condition of Johnson and Jackson [24] is used to calculate the tangential velocity and granular temperature of the solid phase on the wall. According to the experimental results, the minimum fluidization condition is determined as the initial condition for the numerical calculation, indicating that the force balance between the buoyancy of suspended solid particles and the drag

force of fluidization gas is achieved. As shown in Figure **5**, the bed height is the same as the experimental minimum fluidized bed height. For CFD-DEM simulation, the required bed height (0.145m) is achieved by setting the inlet gas velocity at 0 to mimic the particle sedimentation to the lower part of the bed.

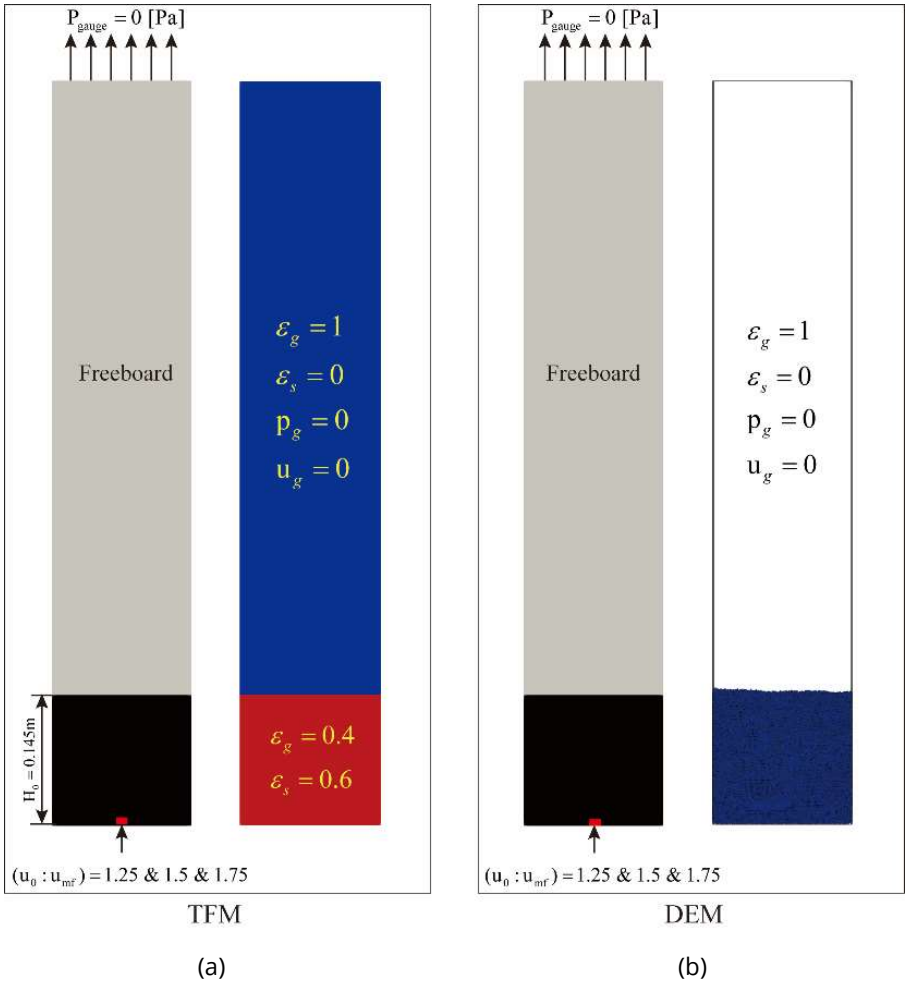

Figure 5: Boundary and initial conditions for the simulations of (a) TFM and (b) DEM.

3.4. Simulation Setting

To conduct the TFM and CFD-DEM simulations, an open-source software MFIX was used. Both models are solved using the Navier-Stokes equations for the continuous (fluid) phase. However, there are different approaches to the discrete particle phase [38]. To analyze the results effectively, we decide to focus on the time average vertical velocity of the particle along the vertical axis of the center. As a result, we are able to assess the accuracy of predictions for the vertical velocity of the particle V_y and the fountain height H_F (corresponding to the point at which V_y becomes zero). It is worth noting that the spouted bed begins to fluidize from static to minimum fluidization velocity u_{mf} with the increase of bottom inlet gas velocity and then to steady-state as assumed. First, we simulate the flow behavior of SFB for two seconds to establish a hydrodynamic state. Then, the simulated data of the steady-state after three seconds are collected and averaged. For CFD-DEM, we inject 62309 spherical particles with a density of 2505 kg/m^3 and a diameter of 2 mm into the bed, and the converted weight is 0.6538 kg, which was consistent with the experimental data. Then, set the inlet gas velocity to 0, simulate 0.5 s to make the particles settle naturally, and get the position information of particles at this time. Finally, compare the different drag models. For TFM, we first compare the effects of different restitution coefficients on the simulation to obtain the optimal values and then study the effects of different friction stress models on spouted bed flow. More corresponding parameters of the TFM and the CFD-DEM are in Table **2** and **3**, respectively.

Table 2: Simulation conditions and input parameters for the TFM

Gas-phase	
Superficial velocity ratio (u_0/u_{mf})	1.25, 1.5 & 1.75
Dynamic viscosity	1.8×10^{-5} kg/(m·s)
Density	1.2005kg/m^3
Solid-phase	
Density	2505kg/m^3
Diameter	0.002m
Restitution coefficient	0.6,0.7,0.8,0.9
Specularity coefficient	0.5 [39]
Solids pressure	Lun *et al*. [22]
Radial distribution	Carnahan-Starling (mono)
Maximum packing limit	0.63
Granular viscosity	Syamal-O'Brien
Granular bulk viscosity	Lun *et al*. [22]
Drag model	Gidaspow [14]
Frictional stress model	Syamlal [35], Sriveastava and Sundaresan (2003) [36]
Solution methods & solver setting	
Temporal discretization	Implicit Euler [40]
Spatial discretization	Superbee
Timestep	10^{-5}s

Table 3: Simulation conditions and input parameters for the discrete element method.

Particle phase	
Total number of particles	63029
(p–p) and (p–w) friction coefficients	0.1
(p-p) and (p-w) normal spring constant	1000N/m
(p-p) and (p-w) damping norm	0.5
Shape of particles	Spherical
Drag model	Gidaspow [14], BVK [15], Koch-Hill [13], Syamlal-O'Brein [32]
Solution methods & solver setting	
Total time	5s
Solver	Red-black sweep

4. Result and Discussion

4.1. Influence of Drag Models on the CFD-DEM

Many scholars have studied particle flow behaviors by CFD-DEM [9,26-29]. However, the choice of drag model is one of the most controversial aspects of CFD-DEM. Most researchers have adopted the Gidaspow model [14], but others have indicated its flaws and made other choices [41]. In this section, we use the CFD-DEM simulation results to compare the predictions by Gidaspow, BVK, Koch-Hill, and Syamlal-O'Brien drag models with the inlet gas velocity of 1.5u_{mf}.

In Figure **6**, the instantaneous particle distribution in the spouted bed is compared with CFD-DEM simulation results by different drag models at t = 5 s. All four drag models show three typical zones (jet zone, annulus zone,

and fountain zone) in the spouted bed. Gidaspow model [14] is consistent with the Syamlal-O'Brien model [32], which is closer to the experimental snapshot, followed by the BVK model [15] and Koch-Hill model [13]. Figure **7** shows that the particle concentration of different drag models in the annulus is very high and close to the packing limit, while the particle concentrations in the fountain and jet zone are relatively small. The difference in simulation results is mainly reflected in the fountain height. Gidaspow [14] and Syamlal-O'Brien drag models [32] have the highest fountain height, followed by Koch-Hill [13] and BVK [15] is the lowest. This is because, in the spouted bed, particles are subjected to various forces such as gravity, drag, and buoyancy. However, drag is the only force that plays a dominant role in the upward motion of particles. According to the drag force models in table **B1**, the selection of different drag force models is affected by the volume fraction of gas and solid particles, and the particle volume fraction in the spouted bed varies from almost zero to the maximum packing limit, resulting in great differences in the momentum transfer between the gas phase and the solid phase. Therefore, the maximum fountain height is also different.

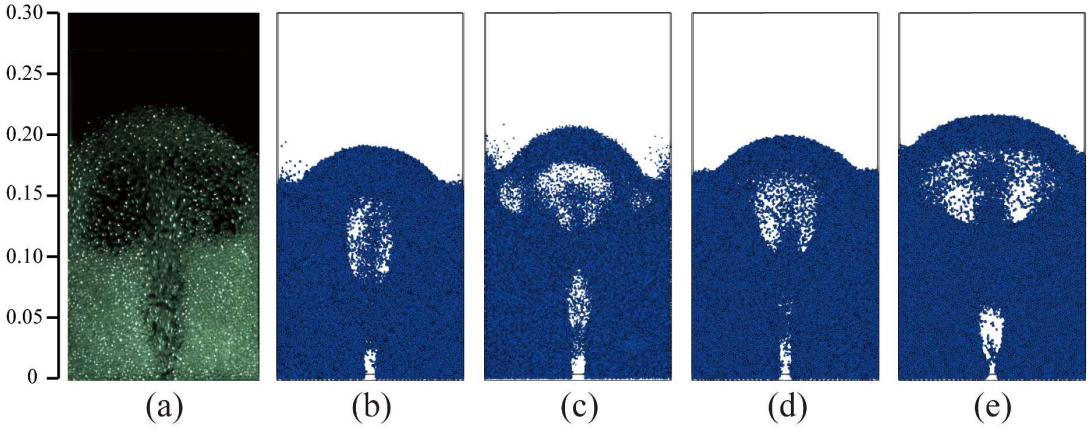

Figure 6: *t*=5s Instantaneous particle distribution in spouted bed with different drag models: (a) Experiment; (b) BVK; (c) Gidaspow; (d) Koch-Hill; (e) Syamlal-O'Brien.

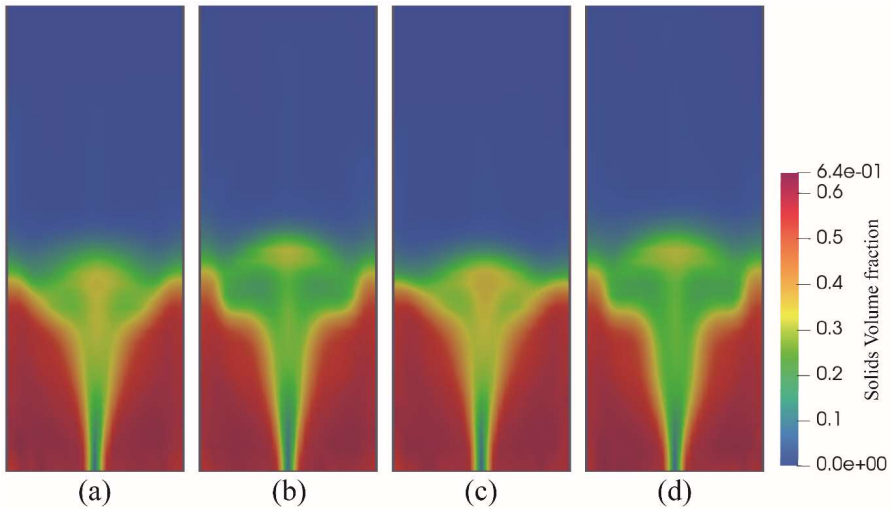

Figure 7: Time-average particle concentration distribution under different drag models: (a) BVK; (b) Gidaspow; (c)Koch-Hill; (d)Syamlal-O'Brien.

As shown in Figure **8**, at the axis of the spouted bed, the particle velocity increases with the increase of the bed height and then decreases with the increase of the bed height. Particle concentration at the top of the fountain decreases to 0, and the height at this point is the fountain height in the spouted bed. The fountain height predicted by the Gidaspow model [14] and Syamal-O'Brien model [32] are almost the same, and they are closer to the experimental data($H_F = 0.205m$) than the BVK model [15] and Koch Hill model [13].

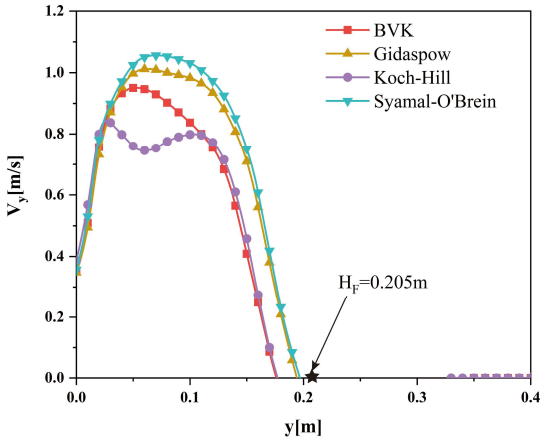

Figure 8: Axial distribution of the time-average vertical velocity of particles under different drag models.

In summary, it can be roughly inferred that the most suitable drag model for this experiment is the Gidaspow drag model [14]. For the inlet gas velocity $u_0 = 1.5u_{mf}$, this resistance model reproduces the flow in the bed (fountain height) better than other models.

4.2. Influence of Parameters on TFM

The influence of the particle-particle restitution coefficient on fluid dynamics in the spouted bed is discussed before studying the influence of different friction stress models. The inlet gas velocity $u_0 = 1.5u_{mf}$ is selected, and the drag force model is the Gidaspow model [14].

4.2.1. Restitution Coefficient

The flow in a gas-solid fluidization system can be divided into three regions according to two critical frictional thresholds of solid volume fraction $\varepsilon_{s,\min}$ and the packing limit $\varepsilon_{s,\max}$ [33]: inertial region $(\varepsilon_s < \varepsilon_{s,\min})$, intermediate regime $(\varepsilon_{s,\min} < \varepsilon_s < \varepsilon_{s,\max})$, and quasi-static regime $(\varepsilon_s > \varepsilon_{s,\max})$. In the inertial region, the fluid flows rapidly, and particles interact mainly by collision. In the intermediate region, particles' momentum is transferred via instantaneous collision and frictional contact. In the quasi-static region, the solid deformation is slow, and particles interact with each other by frictional contact [42]. The fountain area of the spouted bed is in the inertial area where the concentration of particles is low, and the flow velocity is high, and particles interact with each other by collision in this area. The restitution coefficient *e* evaluates the collision effect between a pair of colliding particles.

This part investigates the effects of the restitution coefficient (0.6,0.7,0.8,0.9) on the spouted bed flow. Furthermore, according to Naser *et al*. [39], specularity coefficient is set to be 0.5. As depicted in Figure **9**, granular temperature increases with the increase of the restitution coefficient, and its conclusion is consistent with Goldschmidt *et al*. [43]. And the predicted fountain height is similar to the experimental height when the coefficient of restitution is 0.9. Moreover, it can be seen in Figure **10** that the simulated particle concentration distributions are sensitive to the values of the restitution coefficient. In particular, the particle concentration in the fountain area increases gradually. Since the energy loss caused by the collision between particles decreases with the increase of *e*, resulting in an increase of the number of particles reaching the fountain area.

In summary, the effect of the coefficient of restitution on the gas-solid two-phase flow behavior in the spouted bed cannot be ignored in simulation, and the restitution coefficient *e* = 0.9 is selected as the benchmark for subsequent simulations.

The measuring levels are located at heights of H=0.07m (a), H=0.14m (b), H=0.17m (c). Axial distribution of the time-averaged particle vertical velocity under different restitution coefficients (d), the fountain height H_F=0.205m measured experimentally in our laboratory.

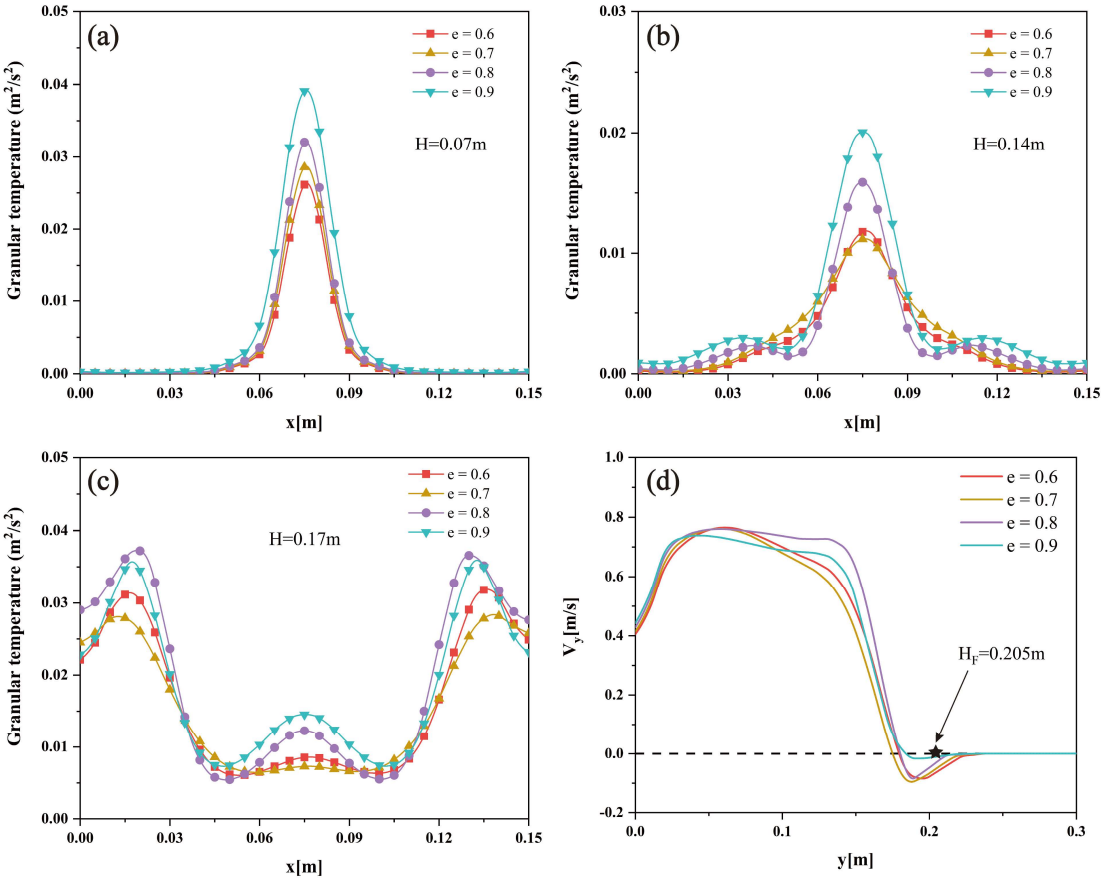

Figure 9: Radial distribution of granular temperature under different restitution coefficients.

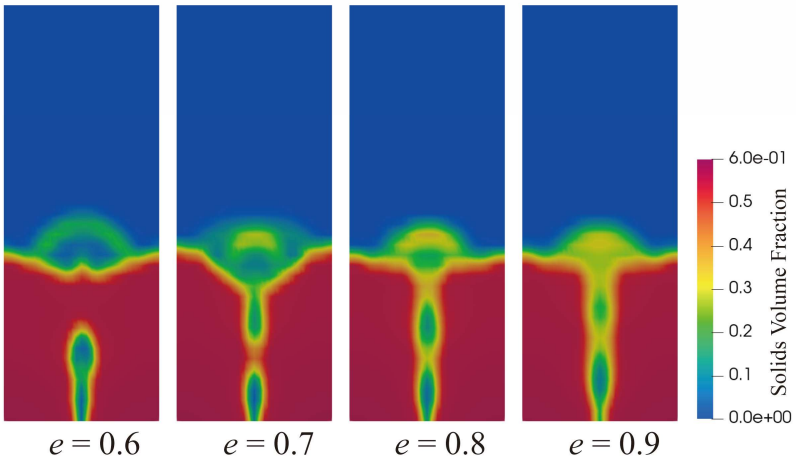

Figure 10: Particle concentration distribution at t=5s under different restitution coefficients.

4.2.2. Frictional Stress Model

For most multiphase flows, gravity and drag are dominant factors, but in the spouted bed, the increasing frictional stress cannot be ignored in dense regions. Different from the complete fluidization of particles in the injection zone, the particles in the annulus are not fluidized, and the flow directions of gas and particles are opposite. The forces among particles are dominated by frictional stress, imposing a crucial influence on the flow behavior in the annulus regime. In addition, the KTGF assumes that there are secondary collisions and instantaneous collisions among particles. When the particle concentration is high, the particle flow cannot be described precisely. It is necessary not only to consider the annulus region (dense particle area) to establish a

suitable model but also to take into account the spouted regime (sparse particle area) to accurately predict the flow behavior in the SFB. In the Srivastava-Sundaresan (S-S) [36] frictional stress model, a transition point with minimum solid concentration $\varepsilon_{s,\min}$ is often used to specify the threshold value of the effective friction state. Generally, the S-S model with $\varepsilon_{s,\min}=0.6$, and $\varepsilon_{s,\min}=0.5$ are employed. We compare both values to test the model's sensitivity to its value. Syamal (S-R-O) [34] model and Only Pressure model (without frictional stress) are also performed in numerical calculations.

According to Figure **11**, the frictional stress model predicted better results than the Only Pressure model. The simulation results can well capture the three zones of the spouted bed flow when employing the frictional stress model. In addition, the solid particle concentration near the bottom wall of the bed calculated by the S-S model is lower than that calculated by the S-R-O model. Particles in the bottom of the bed have obvious downward movement, indicating a better circulation effect and mixing effect. Moreover, when the threshold value $\varepsilon_{s,\min}=0.6$, the simulation result is better than that predicted by $\varepsilon_{s,\min}=0.5$.

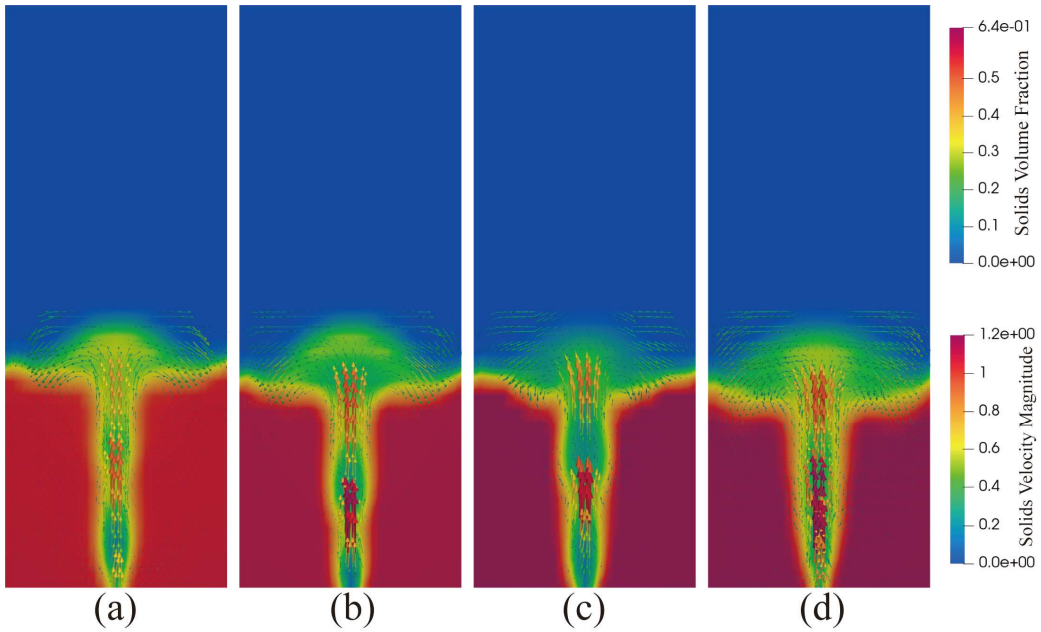

Figure 11: Distribution of particle volume fraction and particle velocity vector at t = 5 s under different frictional stress models: (a) S-S, $\varepsilon_{s,\min}$ =0.5; (b) S-S, $\varepsilon_{s,\min}$ =0.6; (c) S-R-O; (d) Only Pressure.

Figure **12** shows the radial distribution of the time-average granular temperature at three heights under different frictional stress models. At the height of 0.07m, the radial distributions of time-average granular temperature calculated by both frictional stress models are similar. It is symmetrical about the jet axis and has an upward convex shape. The closer to the jet axis, the particles are more affected by the high velocity of the gas phase. Particles near the walls are less sensitive to the jet flow. When the particle concentration is higher, particles are difficult to move, as shown in Figure **12**.

One can also find from Figure **12d** that particles accelerate rapidly near the entrance to reach the maximum velocity at the top of the nozzle area. Particle velocity becomes stabilized gradually after reaching the fountain area and finally decreases to zero. The predicted particle axial velocity is the largest in the acceleration area when the friction stress model is not considered. There is still a significant velocity change in the fountain area compared with the frictional stress models, which is not consistent with the actual situation. There are obvious changes in the prediction results of the S-S model with different transition points $\varepsilon_{s,\min}$, indicating that the transition point value needs to be carefully selected. In addition, the height of the fountain zone predicted by the S-S model with $\varepsilon_{s,\min}$=0.6 is closer to the experimental data. Thus the frictional stress should be considered. Compared with the S-S model, the S-R-O model underestimates the velocity of the particles.

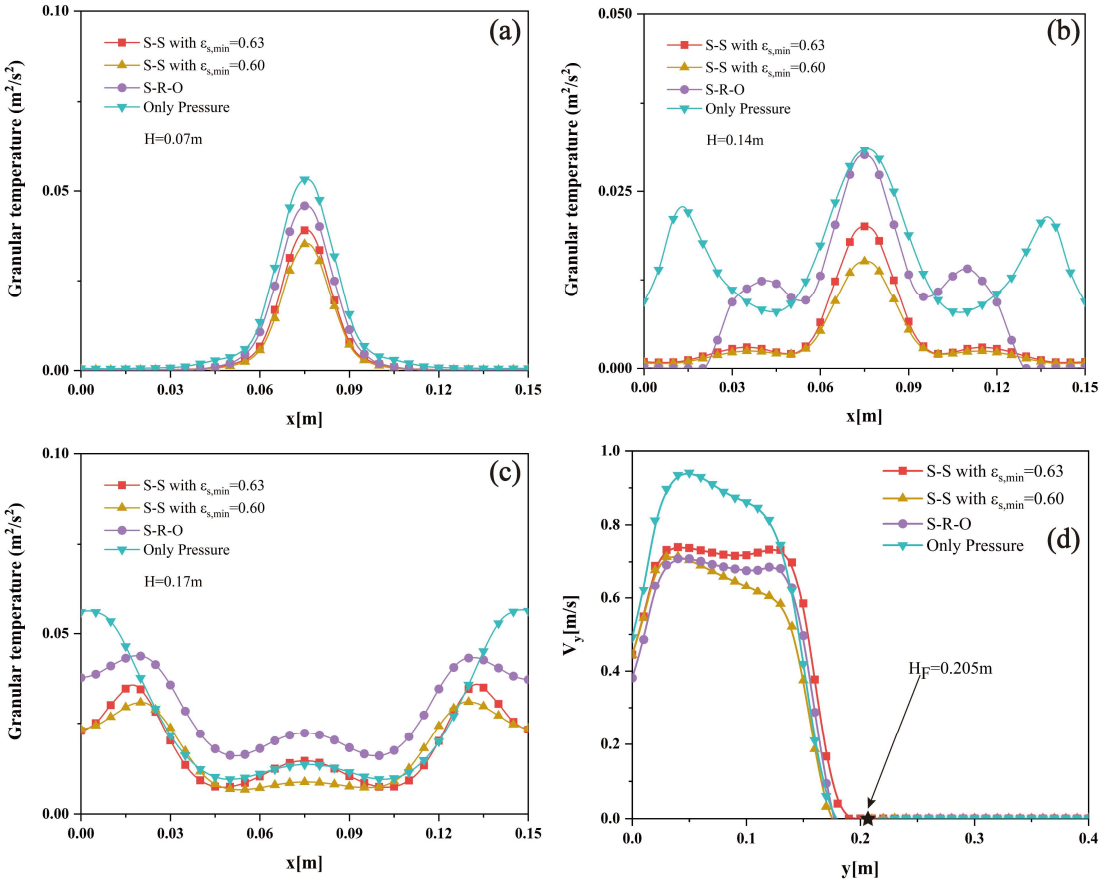

Figure 12: Radial distribution of granular temperature at different heights (H=0.07m (a), H=0.14m(b), H=0.17m(c)) & Time-average particle axial velocity distribution along the axial direction predicted by combining different frictional stress models (d).

4.3. Comparison of Euler–Euler and Euler–Lagrange Models

After optimizing the results in the previous section, we now focus on the study of spouted fluidized bed flow behavior at three gas velocities. Here, the numerical simulation results obtained by TFM and CFD-DEM are compared with the experimental results. Firstly, a comparison of the overall bed flow behavior is carried out, and then the fountain height is evaluated in terms of the particle axial velocity distribution.

In order to verify the numerical results obtained from TFM and CFD-DEM, Figures **13**, **14**, and **15** show different degrees of details of particle velocity and concentration distributions predicted by TFM and CFD-DEM. As air enters the fluidized bed, the overall bed expands, and a small bubble forms at the inlet. The particle concentration above the bubble decreases, and the particle velocity increases with time. As one can find, the simulation results of TFM and CFD-DEM have good similarities when the inlet gas velocity is 1.25 u_{mf} . However, with the increase of inlet gas velocity, the bubble size and bed height predicted by the CFD-DEM is larger than that predicted by TFM. Due to the increase of inlet gas velocity, the interaction between gas and particles is strengthened, forming a dilute-top/dense-bottom structure [44]. In such a structure, the gas-solid drag coefficient will increase due to the block of the gas phase pathway. However, the current TFM fails to predict this phenomenon well. Combined with the velocity vector distribution of TFM, the predicted solid velocity is lower, and the drag coefficient is higher at the top of the bed, which makes the predicted bed height to be less than that of CFD-DEM predictions. At the junction of gas and particles inside the bed, particles interact with the gas and then fall down near the wall to accumulate at the bottom of the bed. The gas-solid slip velocity predicted by TFM near the wall is higher, and the drag coefficient is reduced in such a structure [45]. Thus the annular core structure formed by TFM is smaller than that of CFD-DEM. Overall, the drag coefficient currently used is based on homogeneous system experiments. With the increase of momentum exchange between gas and solid, these drag correlations are no longer applicable to heterogeneous flows and easily result in a poor prediction result[45].

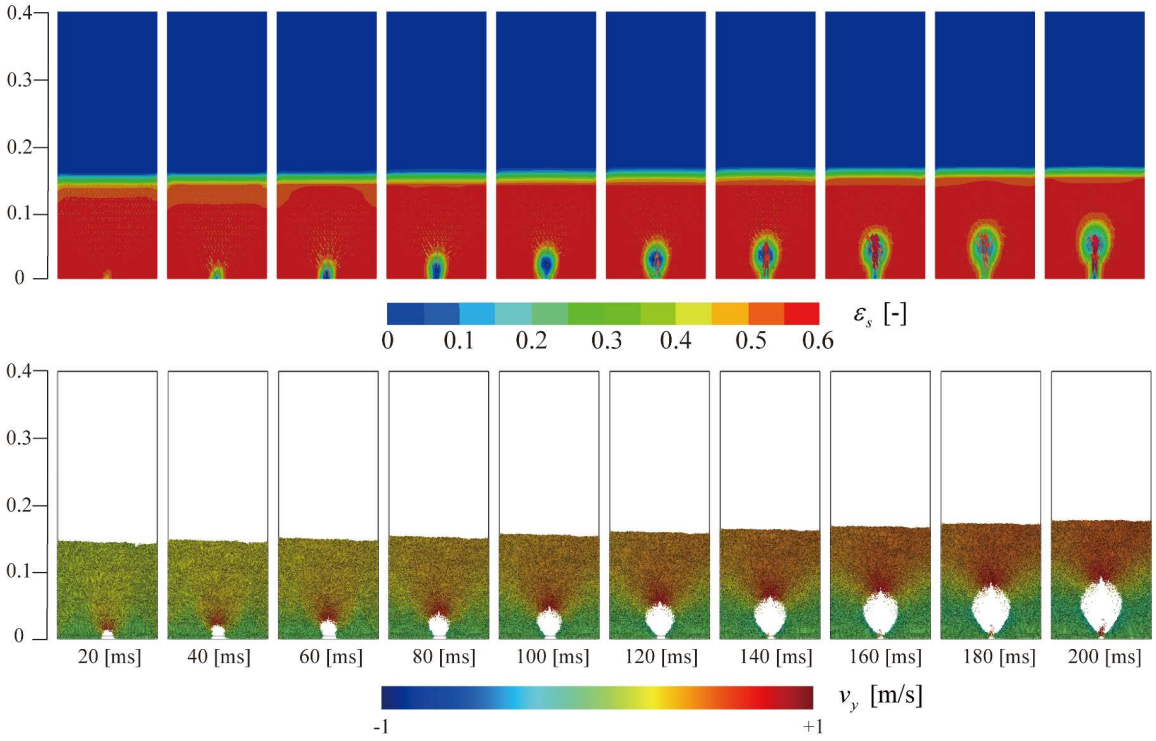

Figure 13: Snapshot of solid phase volume fraction and velocity vector at the gas velocity of 1.25u_{mf} from 0 to 200ms: TFM (upper row); CFD-DEM (lower row) (vertical component of the particle velocity predicted by the CFD-DEM and TFM velocity vector).

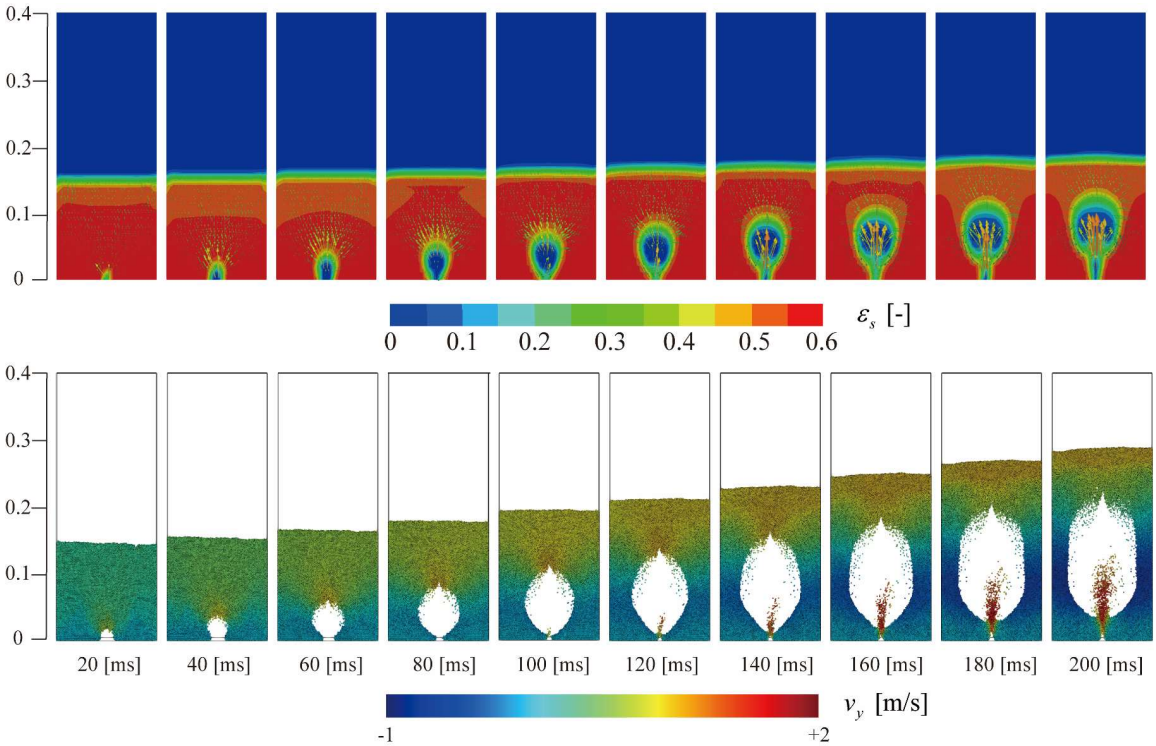

Figure 14: Snapshot of solid phase volume fraction and velocity vector at the gas velocity of 1.50u_{mf} from 0 to 200ms: TFM (upper row); CFD-DEM (lower row) (vertical component of the particle velocity predicted by the CFD-DEM and TFM velocity vector).

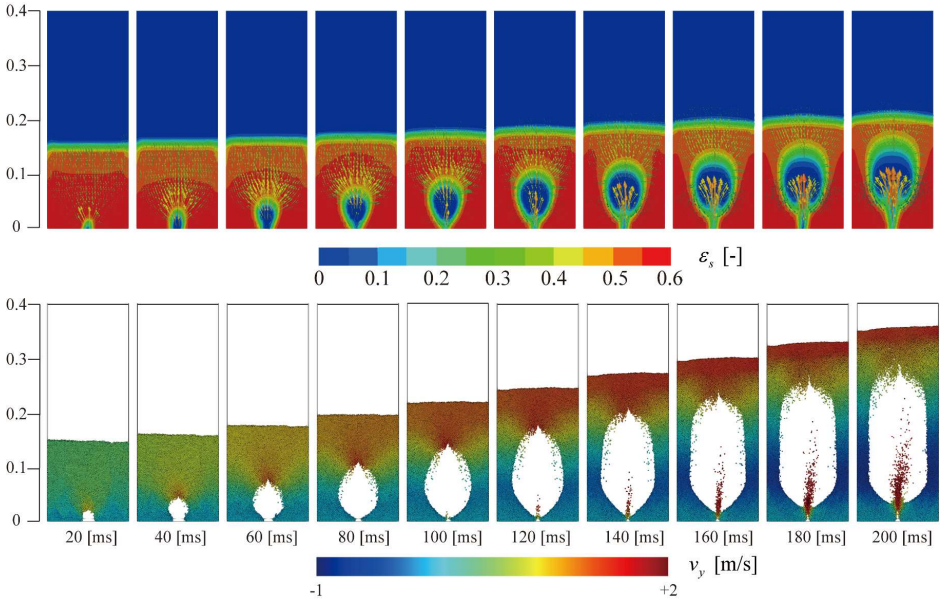

Figure 15: Snapshot of solid phase volume fraction and velocity vector at the gas velocity of 1.75u_{mf} from 0 to 200ms: TFM (upper row); CFD-DEM (lower row) (vertical component of the particle velocity predicted by the CFD-DEM and TFM velocity vector).

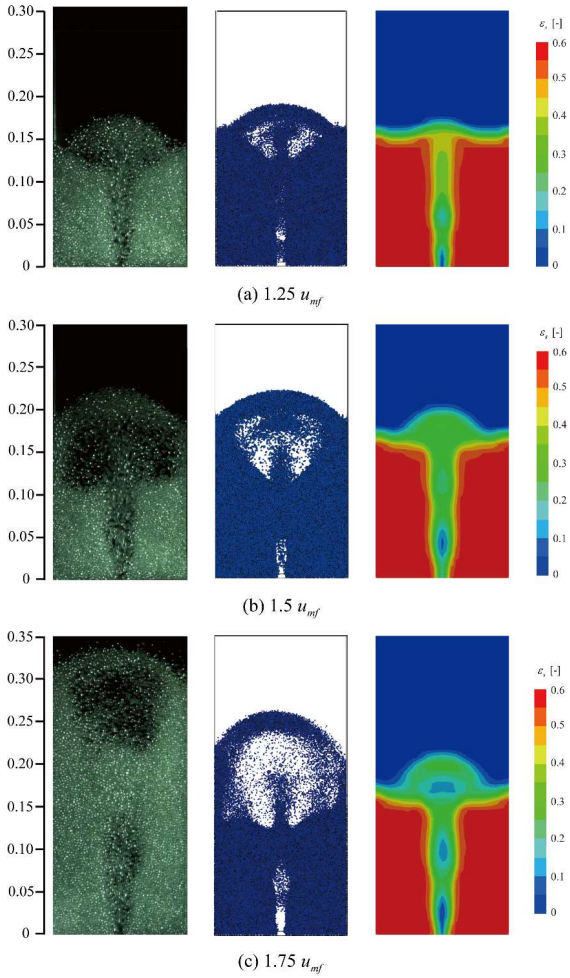

Figure 16: Comparison of instantaneous particle distribution between experimental results (left), CFD-DEM (middle) and TFM (right) at three different superficial gas velocities: (a) 1.25u_{mf} (b)1.5u_{mf} (c)1.75u_{mf}

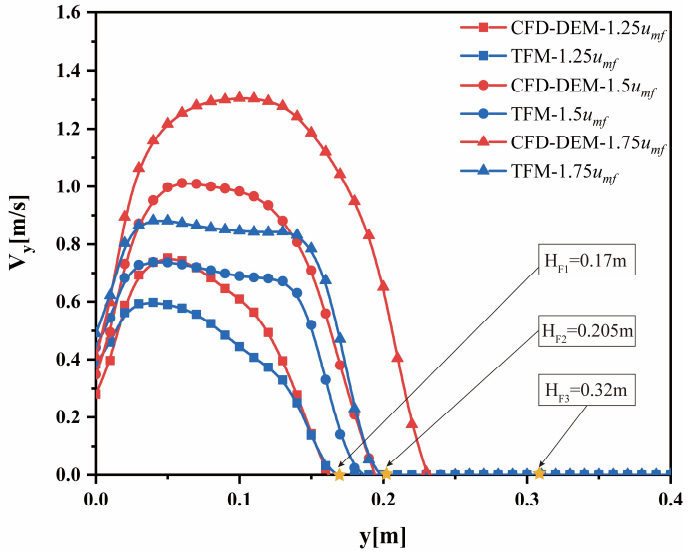

Figure 17: Axial velocity distribution of particles in CFD-DEM and TFM at different gas velocities.

The fountain height H_{F1} = 0.17m (1.25u_{mf}), H_{F2} = 0.205m(1.5u_{mf}) and H_{F3} = 0.32m(1.75u_{mf}) are measured experimentally.

The instantaneous particle distribution calculated by the TFM and CFD-DEM methods is compared with the experimental snapshot results, as shown in Figure **16**. According to Moliner *et al*. [8], since the CFD-DEM calculated the motion of particles alone, it can easily track the trajectory of particles and provide detailed information of particles' motion; thus, the predicted solid volume fraction is closer to the experimental value.

To quantitatively analyze the prediction of fountain height by TFM and CFD-DEM, the axial distributions of particle velocity in both methods under different gas velocities are analyzed. The fountain height calculated by TFM is lower than that calculated by CFD-DEM, and the fountain height calculated by CFD-DEM is closer to the experimental data, proving that the CFD-DEM has higher accuracy in predicting the flow behaviors in a gas-solid system. This concept is illustrated in Figure **17**.

5. Conclusion

In this paper, a three-dimensional spouted bed is studied via both experiment and numerical simulation. TFM and CFD-DEM are employed to simulate the flow behavior in SFB. Predicted characteristics of the gas-solid two-phase flow are compared with experimental data to evaluate different models. The main conclusions are as follows:

1. The drag model has a great influence on the simulation of particle flow behavior. The fountain height and particle flow behavior predicted by Gidaspow [14] model in the CFD-DEM approach are closer to the experimental results.
2. The frictional stress model has a significant impact on the predicted flow behavior. In TFM, the Gidaspow [14] drag model is selected to study the fluid mechanics of existing spouted beds to evaluate the effect of frictional stress models. The restitution coefficient of 0.9 provides a better prediction, and the S-S model with $\varepsilon_{s,\min} = 0.6$ presents better predictions of particle flow behavior in the SFB.
3. At low superficial gas velocity, the simulated particle distribution of CFD-DEM and TFM are in good agreement with the experimental results. The deviation deteriorates with the increase of superficial gas velocity in the center. The poor prediction results of TFM at higher gas velocities may attribute to the non-uniform flow structure that affects the accurate prediction of the drag coefficient at the top of the bed and near the inner wall of the bubble.

CRediT Authorship Contribution Statement

Xinyao Guo: Conceptualization, Methodology, Software, Writing - original draft, Investigation, Visualization. Guodong Liu: Resources, Formal analysis, Validation, Methodology, Writing - review & editing, Supervision. Junnan Zhao: Experiments, writing – review & editing. Runchun Wang: Data curation. Yurong He: Writing – review & editing, Supervision.

Declaration of Competing Interest

The authors declare that they have no known competing financial interests or personal relationships that could have influenced the work reported in this paper.

Acknowledgment

This work was supported by the Natural Science Foundation of China through Grant No. 51776058.

Nomenclature

Latin Symbols

$\vec{u}_g, \vec{u}_s$	Velocity vector for gas and solid, respectively
p_g, p_s	Pressure for gas and solid
d_s	Particle diameter
C_D	The drag coefficient for a single particle
Re_s	Particle Reynolds number
g_0	Radial distribution function
β_{gs}	Interphase momentum exchange coefficient
H	Height
$\overline{\overline{I}}$	Unit tensor
e	Restitution coefficient
$\vec{u}_{mf}$	Minimum fluidization velocity
$\vec{u}_0$	Inlet gas velocity
$\overline{\overline{D}}_s$	Deviatoric rate-of-strain tensor
N	The number of particles in the computational cell

Greek Symbols

$\varepsilon_g, \varepsilon_s$	Concentration for gas and solid phase, respectively
ρ_g, ρ_s	Density for gas and solid phase, respectively
$\overline{\overline{\tau}}_g, \overline{\overline{\tau}}_s$	Stress tensor for gas and solid phase, respectively
$\varepsilon_{s,\min}$	Threshold volume fraction for friction
$\varepsilon_{s,\max}$	Maximum solid volume fraction at packing

θ	Granular temperature
κ_s	Diffusion coefficient
γ_s	The conductivity of granular fluctuating energy
$\vec{f}_{ij}$	The contact force between particle *i* and *j*
$\vec{F}_{drag}$	Drag force

Subscript

g	Gas phase
s	Solid phase

Superscript

n	Normal component
t	Tangential component

Abbreviations

SFB	Spout Fluidized Bed
TFM	Two-fluid model
CFD-DEM	Computational fluid dynamics-discrete element method
S-R-O	Syamlal frictional stress model
S-S	Srivastava-Sundaresan frictional stress model
KTGF	Kinetic theory of granular flow
BVK	Beetstra *et al*. drag model
MFIX	Multiphase Flow with Interphase eXchanges

References

[1] Kunii D, Levenspiel O. Fluidization engineering [M]. Butterworth-Heinemann, 1991.

[2] Mathur KB, Epstein N. Dynamics of spouted beds,Advances in Chemical Engineering: Elsevier, 1974; 111-191. https://doi.org/10.1016/S0065-2377(08)60286-0

[3] Belhocine A. Numerical study of heat transfer in fully developed laminar flow inside a circular tube [J]. The International Journal of Advanced Manufacturing Technology, 2016; 85 (9): 2681-2692. https://doi.org/10.1007/s00170-015-8104-0

[4] Ding J, Gidaspow D. A bubbling fluidization model using kinetic theory of granular flow [J]. AIChE journal, 1990; 36 (4): 523-538. https://doi.org/10.1002/aic.690360404

[5] Gidaspow D, Jung J, Singh RK. Hydrodynamics of fluidization using kinetic theory: an emerging paradigm: 2002 Flour-Daniel lecture [J]. Powder Technology, 2004; 148 (2-3): 123-141. https://doi.org/10.1016/j.powtec.2004.09.025

[6] Cundall PA, Strack OD. A discrete numerical model for granular assemblies [J]. geotechnique, 1979; 29 (1): 47-65. https://doi.org/10.1680/geot.1979.29.1.47

[7] Tsuji Y, Kawaguchi T, Tanaka T. Discrete particle simulation of two-dimensional fluidized bed [J]. Powder technology, 1993; 77 (1): 79-87. https://doi.org/10.1016/0032-5910(93)85010-7

[8] Moliner C, Marchelli F, Spanachi N, *et al.* CFD simulation of a spouted bed: Comparison between the Discrete Element Method (DEM) and the Two Fluid Model (TFM) [J]. Chemical Engineering Journal, 2019; 377: 120466. https://doi.org/10.1016/j.cej.2018.11.164

[9] Zhao X-L, Li S-Q, Liu G-Q, *et al.* DEM simulation of the particle dynamics in two-dimensional spouted beds [J]. Powder Technology, 2008; 184 (2): 205-213. https://doi.org/10.1016/j.powtec.2007.11.044

[10] Saidi M, Tabrizi HB, Grace JR, *et al.* Hydrodynamic investigation of gas-solid flow in rectangular spout-fluid bed using CFD-DEM modeling [J]. Powder Technology, 2015; 284: 355-364. https://doi.org/10.1016/j.powtec.2015.07.005

[11] Marchelli F, Moliner C, Bosio B, *et al.* A CFD-DEM sensitivity analysis: The case of a pseudo-2D spouted bed [J]. Powder Technology, 2019; 353: 409-425. https://doi.org/10.1016/j.powtec.2019.05.035

[12] Li L, Li B, Liu Z. Modeling of spout-fluidized beds and investigation of drag closures using OpenFOAM [J]. Powder Technology, 2017; 305: 364-376. https://doi.org/10.1016/j.powtec.2016.10.005

[13] Koch D L, Hill R J. Inertial effects in suspension and porous-media flows [J]. Annual Review of Fluid Mechanics, 2001; 33 (1): 619-647. https://doi.org/10.1146/annurev.fluid.33.1.619

[14] Gidaspow D. Multiphase flow and fluidization: continuum and kinetic theory descriptions[M]. Academic press, 1994.

[15] Beetstra R, Van Der Hoef MA, Kuipers J. Drag force of intermediate Reynolds number flow past mono-and bidisperse arrays of spheres [J]. AIChE journal, 2007; 53 (2): 489-501. https://doi.org/10.1002/aic.11065

[16] Pietsch S, Heinrich S, Karpinski K, *et al.* CFD-DEM modeling of a three-dimensional prismatic spouted bed [J]. Powder technology, 2017; 316: 245-255. https://doi.org/10.1016/j.powtec.2016.12.046

[17] Estiati I, Tellabide M, Saldarriaga J, *et al.* Fine particle entrainment in fountain confined conical spouted beds [J]. Powder Technology, 2019; 344: 278-285. https://doi.org/10.1016/j.powtec.2018.12.035

[18] Du W, Bao X, Xu J, *et al.* Computational fluid dynamics (CFD) modeling of spouted bed: Assessment of drag coefficient correlations [J]. Chemical Engineering Science, 2006; 61 (5): 1401-1420. https://doi.org/10.1016/j.ces.2005.08.013

[19] Du W, Bao X, Xu J, *et al.* Computational fluid dynamics (CFD) modeling of spouted bed: Influence of frictional stress, maximum packing limit and coefficient of restitution of particles [J]. Chemical Engineering Science, 2006; 61(14): 4558-4570. https://doi.org/10.1016/j.ces.2006.02.028

[20] Moliner C, Marchelli F, Ong L, *et al.* Sensitivity analysis and validation of a Two Fluid Method (TFM) model for a spouted bed [J]. Chemical Engineering Science, 2019; 207: 39-53. https://doi.org/10.1016/j.ces.2019.06.008

[21] Stroh A, Alobaid F, Hasenzahl MT, *et al.* Comparison of three different CFD methods for dense fluidized beds and validation by a cold flow experiment [J]. Particuology, 2016; 29: 34-47. https://doi.org/10.1016/j.partic.2015.09.010

[22] Lun C, Savage S B, Jeffrey D, *et al.* Kinetic theories for granular flow: inelastic particles in Couette flow and slightly inelastic particles in a general flowfield [J]. Journal of fluid mechanics, 1984; 140: 223-256. https://doi.org/10.1017/S0022112084000586

[23] Carnahan NF, Starling KE. Equation of state for nonattracting rigid spheres [J]. The Journal of chemical physics, 1969; 51 (2): 635-636. https://doi.org/10.1063/1.1672048

[24] Johnson PC, Jackson R. Frictional-collisional constitutive relations for granular materials, with application to plane shearing [J]. Journal of fluid Mechanics, 1987; 176: 67-93. https://doi.org/10.1017/S0022112087000570

[25] Xu B, Yu A. Numerical simulation of the gas-solid flow in a fluidized bed by combining discrete particle method with computational fluid dynamics [J]. Chemical Engineering Science, 1997; 52 (16): 2785-2809. https://doi.org/10.1016/S0009-2509(97)00081-X

[26] GoTz SR. Gekoppelte CFD/DEM-simulation blasenbildender wirbelschichten[M]. Shaker, 2006.

[27] Liu G, Yu F, Lu H, *et al.* CFD-DEM simulation of liquid-solid fluidized bed with dynamic restitution coefficient [J]. Powder Technology, 2016; 304: 186-197. https://doi.org/10.1016/j.powtec.2016.08.058

[28] Liu G, Yu F, Wang S, *et al.* Investigation of interstitial fluid effect on the hydrodynamics of granular in liquid-solid fluidized beds with CFD-DEM [J]. Powder Technology, 2017; 322: 353-368. https://doi.org/10.1016/j.powtec.2017.08.048

[29] Zhao J, Shan T. Coupled CFD-DEM simulation of fluid-particle interaction in geomechanics [J]. Powder technology, 2013; 239: 248-258. https://doi.org/10.1016/j.powtec.2013.02.003

[30] Ergun S. Fluid flow through packed columns [J]. Chem. Eng. Prog., 1952; 48: 89-94.

[31] Wen CY. Mechanics of fluidization [C]. Chem. Eng. Prog. Symp. Ser., 1966: 100-111.

[32] Syamlal M, O'brien T. Simulation of granular layer inversion in liquid fluidized beds [J]. International Journal of Multiphase Flow, 1988; 14 (4): 473-481. https://doi.org/10.1016/0301-9322(88)90023-7

[33] Ancey C. Plasticity and geophysical flows: a review [J]. Journal of Non-Newtonian Fluid Mechanics, 2007; 142 (1-3): 4-35. https://doi.org/10.1016/j.jnnfm.2006.05.005

[34] Syamlal M, Rogers W, Obrien TJ. MFIX documentation theory guide[R]. USDOE Morgantown Energy Technology Center, WV (United States), 1993. https://doi.org/10.2172/10145548

[35] Schaeffer DG. Instability in the evolution equations describing incompressible granular flow [J]. Journal of differential equations, 1987; 66 (1): 19-50. https://doi.org/10.1016/0022-0396(87)90038-6

[36] Srivastava A, Sundaresan S. Analysis of a frictional-kinetic model for gas-particle flow [J]. Powder technology, 2003; 129 (1-3): 72-85. https://doi.org/10.1016/S0032-5910(02)00132-8

[37] Geldart D. Types of gas fluidization [J]. Powder technology, 1973; 7 (5): 285-292. https://doi.org/10.1016/0032-5910(73)80037-3

[38] Lungu M, Siame J, Mukosha L. Comparison of CFD-DEM and TFM approaches for the simulation of the small scale challenge problem 1 [J]. Powder Technology, 2021; 378: 85-103. https://doi.org/10.1016/j.powtec.2020.09.071

[39] Almohammed N, Alobaid F, Breuer M, *et al.* A comparative study on the influence of the gas flow rate on the hydrodynamics of a gas-solid spouted fluidized bed using Euler-Euler and Euler-Lagrange/DEM models [J]. Powder technology, 2014; 264: 343-364. https://doi.org/10.1016/j.powtec.2014.05.024

[40] Belhocine A, Omar WZW. Analytical solution and numerical simulation of the generalized Levèque equation to predict the thermal boundary layer [J]. Mathematics and Computers in Simulation, 2021; 180: 43-60. https://doi.org/10.1016/j.matcom.2020.08.007

[41] Moliner C, Marchelli F, Bosio B, *et al.* Modelling of Spouted and Spout-Fluid Beds: Key for Their Successful Scale Up [J]. Energies, 2017; 10 (11): 1729. https://doi.org/10.3390/en10111729

[42] Zhao J, Liu G, Li W, *et al.* A comprehensive stress model for gas-particle flows in dense and dilute regimes [J]. Chemical Engineering Science, 2020; 226: 115833. https://doi.org/10.1016/j.ces.2020.115833

[43] Goldschmidt M, Kuipers J, Van Swaaij WPM. Hydrodynamic modelling of dense gas-fluidised beds using the kinetic theory of granular flow: effect of coefficient of restitution on bed dynamics [J]. Chemical Engineering Science, 2001; 56 (2): 571-578. https://doi.org/10.1016/S0009-2509(00)00262-1

[44] Jinghai L, Musun G. Heterogeneity in Vertical Cocurrent-Up Particle-Fluid Two Phase Flow [J]. Journal of Chemical Industry and Engineering (China), 1993; 1.

[45] Yang N, Wang W, Ge W, *et al.* CFD simulation of concurrent-up gas-solid flow in circulating fluidized beds with structure-dependent drag coefficient [J]. Chemical Engineering Journal, 2003; 96 (1-3): 71-80. https://doi.org/10.1016/j.cej.2003.08.006